Density-functional theory and triply-periodic minimal surfaces

Mengdi Yin (尹梦迪), Jing Zhang (张璟), and Dimitri D. Vvedensky
The Blackett Laboratory, Imperial College London, London SW7 2AZ, United Kingdom

(Received 26 February 2025; revised 12 June 2025; accepted 17 June 2025; published 7 July 2025)

Several authors have suggested that the surfaces of vanishing potential generated by the electrostatic fields from a periodic distribution of point charges resemble triply-periodic minimal surfaces (TPMS) whose symmetry corresponds to the positions of the point charges. We provide an alternative theory based on the quantum mechanical charge density ρ, rather than the classical discrete charges used in previous work. The Boltzmann equation is used to show that surfaces of $\rho = 0$ correspond to minimal surfaces, which, for periodic systems, are TPMS. We then use density-functional calculations for elemental materials that differ electronically and structurally, namely, Na, Cu, and Al, to show that surfaces for which $\varrho \to 0$ converge to the TPMS corresponding to the crystalline material.

DOI: 10.1103/trld-8v8h

I. INTRODUCTION

Surfaces that minimize their area for given boundary conditions are called minimal surfaces. Historically, the concept of a minimal surface was proposed for the formation of a soap film, requiring the minimization of the surface free energy, which is proportional to the surface area [1,2].

The local shape near a point of a smooth three-dimensional surface is determined by the principal curvatures k_1 and k_2 which are the maximum and minimum bending near that point. The local geometry of the surface is characterized by the mean curvature $M = \frac{1}{2}(k_1 + k_2)$ and the Gaussian curvature $K = k_1 k_2$ [1,3]. Minimal surfaces with given boundaries have minimal free energy, such that the minimal surface area is ensured by the condition $M = 0$ [1,3]. The catenoid (the surface of revolution of a catenary) is a standard example of a minimal surface.

Minimal surfaces with repeating units in three independent directions are called triply-periodic minimal surfaces (TPMS) [4,5]. Sections of TPMS for body-centered and face-centered cubic lattices are shown in Fig. 1. There are two basic uses of TPMS. The first utilizes the high surface-to-volume and strength-to-weight ratios, tunable mechanical properties, porosity, and other characteristics of TPMS [6] to explore applications, especially with additive manufacturing (three-dimensional printing) [7,8]. Examples include engineered [9] and biomimetic scaffolds [10], architecture and interior design [11], thermomechanical materials [12], thermal management [13], and carbon allotropes [14]. Many such applications are based on minimal surfaces found in nature [15–17].

The second use of minimal surfaces is in fundamental studies, where they appear in a broad range of problems in mathematics [18,19] and physics, biology, and materials science. The shape and curvature of minimal surfaces have also been used as organizing principles for synthetic and biological assemblies [1,20,21]. Hyde and Andersson [22,23] were the first to apply TPMS to model the initial and final states of the martensitic transformation in iron. We have extended these ideas to other materials by regarding the martensitic transformation as a topological transformation. If the intermediate states are also in the TPMS family, the material exhibits the shape memory effect, that is, the material recovers from an initial plastic deformation in a low-temperature phase to its original shape upon heating above a transformation temperature. We have discussed these ideas in [24], but a more complete discussion will be presented elsewhere.

Several authors [25–29] have suggested that TPMS are approximated by nodal surfaces of Fourier series, or as the zero equipotential surfaces of distributions of point charges. The main advantage of the Fourier method is that, to leading order, TPMS are approximated by algebraic combinations of trigonometric functions [26]. These expressions are much easier to display and manipulate than the exact forms of TPMS, as obtained from the Weierstrass representation [30] or from the Allen-Cahn equation [31].

Here, we take a different approach to determining the TPMS associated with a crystalline material by utilizing the quantum mechanical charge density ρ, which includes exchange and correlation. The Boltzmann equation is first used to provide a semiclassical proof that the surface corresponding to $\rho = 0$ is a minimal surface. We then use calculations based on density-functional theory (DFT) to determine surfaces of constant charge density for crystalline Na, Al, and Cu. We show that the surfaces of constant ρ do indeed converge to the TPMS of the structure for these materials as $\rho \to 0$. We will show elsewhere that these results can be extended to other materials and to other crystalline structures of the materials studied here. Our calculations provide a direct association between minimal surfaces and crystalline materials that can be used to study their topological properties and solid-state transitions.

Published by the American Physical Society under the terms of the Creative Commons Attribution 4.0 International license. Further distribution of this work must maintain attribution to the author(s) and the published article's title, journal citation, and DOI.

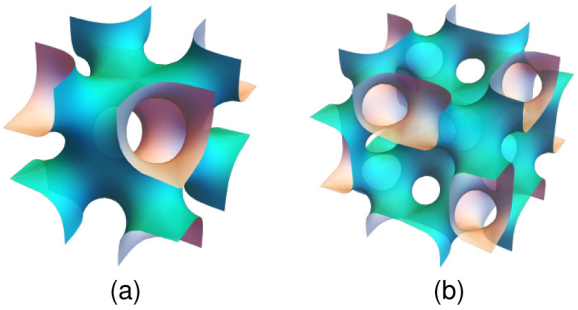


FIG. 1. Periodic units that repeat along three independent directions to form a TPMS: (a) the I-WP surface, for body-centered cubic (BCC) lattices, and (b) the F-RD surface, for face-centered cubic (FCC) lattices.

II. MINIMAL CHARGE DENSITY SURFACES

We begin with the semiclassical transport theory based on the Boltzmann equation [32],

$$\frac{\partial f}{\partial t} + \frac{q\boldsymbol{F}}{\hbar} \cdot \nabla_{\boldsymbol{k}} f + \boldsymbol{v} \cdot \nabla_{\boldsymbol{x}} f = Q(f), \tag{1}$$

where $f(\boldsymbol{x}, \boldsymbol{k}, t)\, d\boldsymbol{x}\, d\boldsymbol{k}$ is the probability of finding a particle in the volume $d\boldsymbol{x}\, d\boldsymbol{k}$ centered at $(\boldsymbol{x}, \boldsymbol{k})$ at time t, q is the charge on the particle, $\boldsymbol{F}$ is an external field, and $Q(f)$ is the collision integral. In the low-density approximation for Q [33], the Boltzmann equation reduces to the continuity equation for the charge density ρ,

$$\frac{\partial \rho}{\partial t} + \nabla \cdot \boldsymbol{j} = 0, \tag{2}$$

where the current density $\boldsymbol{j}$ is the sum of drift $\boldsymbol{j}_F$ and diffusion $\boldsymbol{j}_D$ current densities:

$$\boldsymbol{j}_F = q\mu\rho\boldsymbol{F}, \quad \boldsymbol{j}_D = qD\nabla\rho. \tag{3}$$

Here, μ is the electron mobility and the Einstein relation [34] is used for the diffusion coefficient D, which is assumed to be spatially homogeneous. In the stationary limit, (2) is replaced by

$$\nabla \cdot \boldsymbol{j} = \nabla \cdot (\boldsymbol{j}_F + \boldsymbol{j}_D) = 0, \tag{4}$$

with the divergences

$$\nabla \cdot \boldsymbol{j}_F = q\mu\nabla\rho \cdot \boldsymbol{F} + q\mu\rho\nabla \cdot \boldsymbol{F}, \tag{5}$$

$$\nabla \cdot \boldsymbol{j}_D = qD\nabla^2\rho. \tag{6}$$

Consider a small section near a point p on a surface of constant charge density (Fig. 2). At p,

$$\partial_x \rho\big|_p = \partial_y \rho\big|_p = 0, \tag{7}$$

where subscript notation is used for partial derivatives, e.g., $\partial_x \equiv \partial/\partial x$ and $\partial_y \equiv \partial/\partial y$. Although Fig. 2 displays the surface near p as a saddle point, our proof makes no assumption about this surface other than corresponding to a constant charge density. We will prove that the surface with $\rho = 0$ is a minimal surface. In particular, (7) is valid for any constant charge density surface.

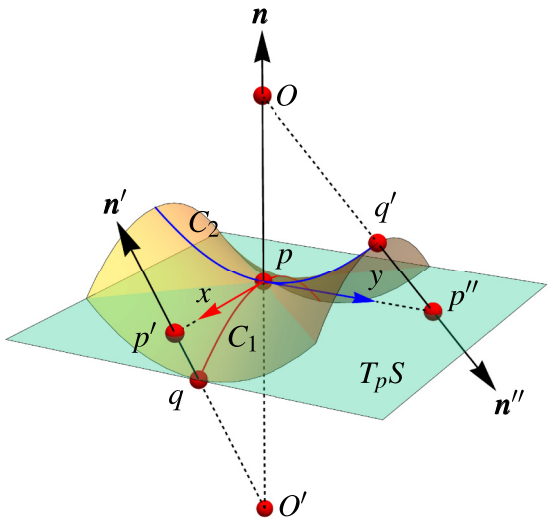


FIG. 2. Region of a surface (shown in yellow) near a point p, curves C_1 and C_2 on the surface along the x and y axes, respectively, and the tangent plane T_pS at p to the surface.

The divergence theorem for $\boldsymbol{j}$ is

$$\iint_S \boldsymbol{j} \cdot d\boldsymbol{S} = \iiint_V \nabla \cdot \boldsymbol{j}\, dV = 0, \tag{8}$$

where $d\boldsymbol{S}$ is the outward normal of surface enclosing the volume V, and (4) is used to evaluate the right-hand side. The left-hand side of (8) is evaluated as an integral over the surface of the pill box centered at p (Fig. 3). Because the tangential components of the current densities are integrated over an area whose width approaches zero, the integral over the sides of the pill box vanish. The normal components of the drift and diffusion current densities are integrated over the top and bottom of the pill box. If these integrals are nonzero, charge either accumulates or is depleted within the pill box. Hence, the invariance of the total charge of the surface enclosed by the pill box gives

$$\partial_{\boldsymbol{n}} j_{\boldsymbol{n}} = 0, \tag{9}$$

where $\partial_{\boldsymbol{n}}$ is the partial derivative with respect to the unit normal $\boldsymbol{n}$ to the surface at p (Fig. 2). Thus, according to (4),

$$\nabla \cdot \boldsymbol{j} = \partial_x \boldsymbol{j}_x + \partial_y \boldsymbol{j}_y, \tag{10}$$

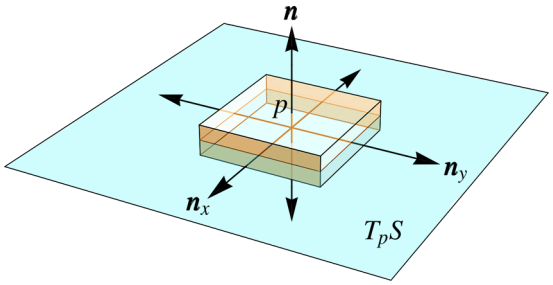


FIG. 3. Thin pill box on the tangent surface T_pS centered at p (Fig. 2) used to calculate the divergence of the drift and diffusion current densities. The outward normals of each section are indicated.

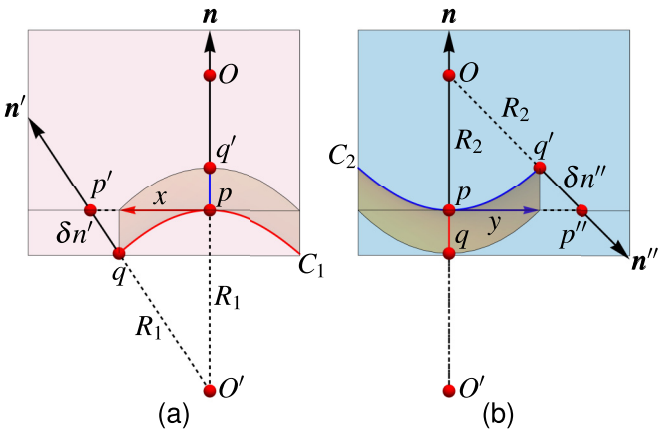


FIG. 4. Sections near the saddle point in Fig. 2 parallel to (a) the x axis and (b) the y axis, with the same labeling. R_1 and R_2 are the radii of circles C_1 and C_2, respectively, that best approximate the surface along the x and y axes. The curvature of the surface along the axes is the reciprocal of the radii.

in which

$$\partial_\alpha \boldsymbol{j}_\alpha = \partial_\alpha \boldsymbol{j}_{\boldsymbol{F},\alpha} + \partial_\alpha \boldsymbol{j}_{D,\alpha}, \tag{11}$$

for $\alpha = x, y$. By using (5)–(7), we have

$$\partial_\alpha \boldsymbol{j}_{\boldsymbol{F},\alpha} = q\mu\rho\partial_\alpha \boldsymbol{F}_\alpha, \tag{12}$$

$$\partial_\alpha \boldsymbol{j}_{D,\alpha} = qD\partial_{\alpha\alpha}\rho. \tag{13}$$

As $\rho \to 0$, then, according to (12), $\partial_\alpha \boldsymbol{j}_\alpha \to 0$, so we are left with (13), which yields

$$\partial_{xx}\rho + \partial_{yy}\rho = 0. \tag{14}$$

The effects of curvature on diffusion are determined by considering the charge density at points p' and p'', which lie on the tangent plane of p, and points q and q', which lie on the surface of constant charge density [Figs. 2 and 4(a)]. By taking Taylor expansions of p' around p ($\delta x = 0$) and q ($\delta n' = 0$), we have

$$\rho(p') \approx \rho(p) + \partial_x\rho\big|_p \delta x + \tfrac{1}{2}\partial_{xx}\rho\big|_p (\delta x)^2 \tag{15}$$

$$\approx \rho(q) + \partial_{n'}\rho\big|_q \delta n', \tag{16}$$

where, because of (7), the first nonvanishing term in (15) is of order $(\delta x)^2$. From Pythagoras' theorem, we have [Fig. 4(a)]

$$(\delta n' + R_1)^2 = R_1^2 + \delta x^2, \tag{17}$$

which yields, to leading order in δx,

$$\delta n' \approx \frac{\delta x^2}{2R_1}. \tag{18}$$

Given that $\rho(p) = \rho(q)$ and $\partial_x\rho|_p = 0$, we have, from (15) and (16),

$$\frac{1}{R_1}\partial'_n\rho|_q = \partial_{xx}\rho|_p. \tag{19}$$

TABLE I. The phases, exchange-correlation (XC) functionals, and the number of mesh grid points used for the calculations reported here.

Material	Phase	XC	FFT Mesh
Na	BCC	LDA	140 × 140 × 140
Cu	FCC	GGA-PBE	100 × 100 × 100
Al	FCC	GGA-PBE	100 × 100 × 100

Similarly, by taking Taylor expansions of p'' about p (δy=0) and q' ($\delta n'' = 0$) [Figs. 2 and 4(b)], we obtain

$$\frac{1}{R_2}\partial_{n''}\rho|_{q'} = \partial_{yy}\rho|_p. \tag{20}$$

As q and q' approach p,

$$\partial_n\rho|_p \approx \partial_{n'}\rho|_q \approx \partial_{n''}\rho|_{q'}. \tag{21}$$

Using (19)–(21), the diffusion terms in (14) can be written as

$$(\partial_{xx}\rho + \partial_{yy}\rho)|_p = -\left(\frac{1}{R_1} + \frac{1}{R_2}\right)\partial_n\rho|_p. \tag{22}$$

According to (14), the left-hand side of this equation must vanish. On the right-hand side, $\partial_n\rho|_p \neq 0$, since the surface is defined by $\rho \to 0$, so nearby surfaces must have $\rho \neq 0$. Thus, the right-hand side vanishes when

$$\frac{1}{R_1} + \frac{1}{R_2} = k_1 + k_2 = 0, \tag{23}$$

where k_1 and k_2 are the principle curvatures at p, so the mean curvature at p is zero. There are several way to write curvatures on surfaces [35]. We conform to the convention where the curvature is positive if the curve turns in the same direction as the surface normal (C_2), and negative otherwise (C_1). Since p is any point on the surface of constant vanishing ρ, the mean curvature vanishes everywhere on this surface, so the surface with $\rho = 0$ is a minimal surface.

III. DENSITY FUNCTIONAL CALCULATIONS

To verify that surfaces of real materials with $\rho = 0$ are minimal, we have used the Vienna *ab initio* simulation package (VASP) [36–39] for materials with different electronic properties. The energy cutoff was set to 520 keV and the **k** spacing was set to 0.02 Å^{-1}. The reciprocal lattice is sampled with a Monkhorst-Pack [40,41] scheme for Na and a Gamma-centered scheme for Al and Cu. Exchange-correlation (XC) functionals and fast Fourier transform (FFT) mesh grids chosen for plotting surfaces of a given charge density are listed in Table I. We use the local density approximation (LDA) [42] for Na, and the nonempirical generalized-gradient-approximation of Perdew, Burke, and Ernzerhof (GGA-PBE) functional [43] for Al and Cu. Lattice parameters were obtained from experiments [44] as the starting points for structural relaxation.

After optimizing the structural parameters of the crystal, we calculate the self-consistent charge density ρ of the ground state from the Kohn-Sham orbitals [45]. Our calculation is conducted over one unit cell, so we set n_{cell} to one and the FFT grid density is the number of grid points that divides the

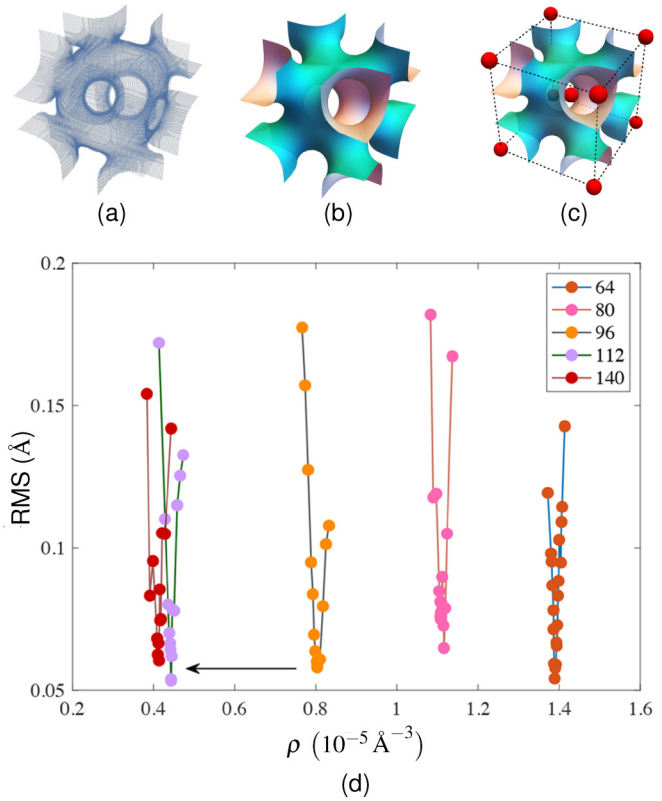


FIG. 5. (a) Charge densities of constant ρ of Na in a BCC lattice. Plot of constant ρ at given values against (b) the I-WP surface. (c) Plot of the BCC lattice against the I-WP TPMS. Red spheres in (c) represent atoms. (d) RMS against charge density ρ of Na in the BCC lattice. The points are where calculations were carried out and the lines are guides for the eye. The arrow points to the minimum of the RMS and the mesh densities are shown in the legend.

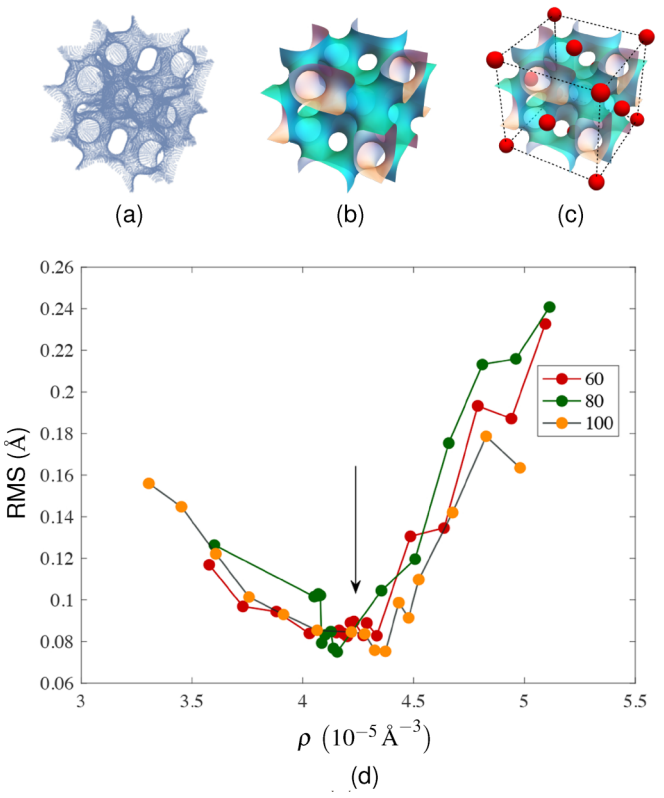


FIG. 6. (a) Charge densities of constant ρ of Al in an FCC lattice. Plot of constant ρ at given values against (b) the F-RD surface. (c) Plots of the FCC and BCC lattice against the F-RD surface. Red spheres in (c) represent atoms. (d) RMS against charge density ρ of Al in the FCC lattice. The points are where calculations were carried out and the lines are guides for the eye. The arrow points to the minimum of the RMS and the mesh densities are shown in the legend.

unit cell in real space. As ρ is a number density, we divide by the crystal volume to obtain the dimension L^{-3}.

We use the root-mean square (RMS) to estimate the deviations of the surfaces of constant charge density S_ρ from its corresponding TPMS, denoted by S. To calculate the RMS, we take a grid of 100×100 mesh points on each elementary piece of the unit cell of the TPMS, from which the entire unit cell can be generated from the operations of the point group. Thus, there are 8×10^4 points on the P surface, 1.6×10^5 points on the I-WP surface, and 3.2×10^5 points on the F-RD surface. S_ρ is formed by n_{ab} points on the FFT mesh with their corresponding charge density ρ falling in an interval $[\rho_a, \rho_b]$. Thus, $\rho \approx \frac{1}{2}(\rho_a + \rho_b)$. We then scale the TPMS, calculate the smallest distance d_i, $i \in n_{ab}$, between each point on S_ρ and S, and establish a data set of the smallest distances, which we use to obtain the RMS. The RMS is calculated as

$$\mathrm{RMS} = \sqrt{\frac{\sum_i^{n_{ab}} d_i^2}{n_{ab}}}. \tag{24}$$

Thus, the lower the dispersion of computed points from its TPMS, the lower the RMS, so the more S_ρ resembles S.

IV. RESULTS

Sodium (Na) is in the first column of the periodic table which, along with the other alkali elements, has a single s electron outside a closed shell. Sodium has atomic number 11, with the electronic configuration $1s^2\,2s^2\,2p^6\,3s^1$. The band structure has a single half-filled $3s$ band, with some $3p$ admixture for higher bands. The bands along the principal directions in $\mathbf{k}$ space are nearly identical, and surfaces of constant energy remain nearly spherical until they are close to the Brillouin zone boundary [46]. Sodium has the BCC structure (space group $Im\bar{3}m$) at room temperature under atmospheric pressure.

Figure 5(d) shows the RMS against the charge density for Na in the BCC lattice for the indicated FFT mesh densities. The data for all plots of the RMS against ρ are available in the SM [30]. The minimum decreases significantly with increasing mesh density and, for all meshes, the RMS shows sharp minima. Convergence with increasing mesh density is clearly evident. The converged minimum of 4.3×10^{-6} Å^{-3} is the best fit obtained. The converged surface is shown in Fig. 5(a), together with the I-WP TPMS corresponding to the BCC lattice of Na in Fig. 5(b), and the positions of the Na atoms against the TPMS in Fig. 5(c). Thus, for BCC Na with

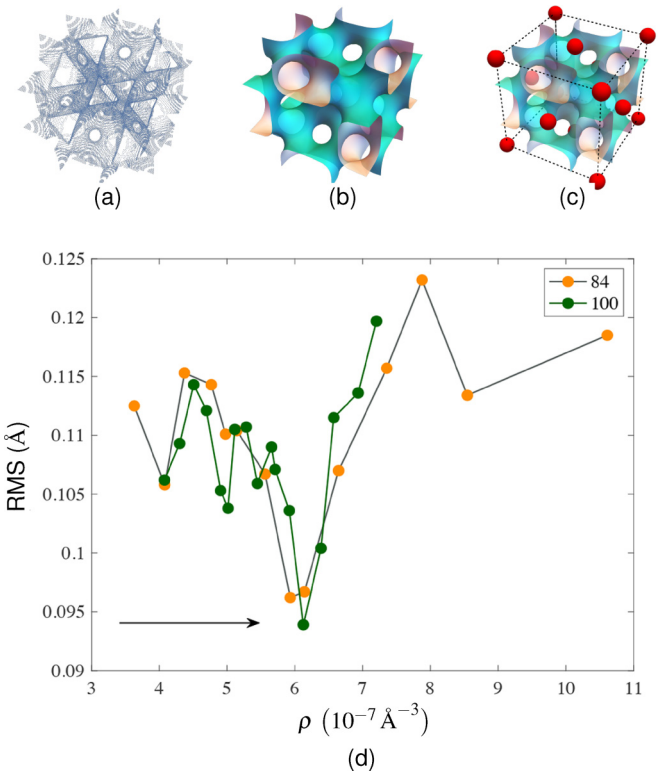


FIG. 7. (a) Charge densities for constant ρ of Cu in an FCC lattice. (b) The F-RD surface. (c) Plots of the FCC lattice against the F-RD TPMS. Red spheres in (c) represent atoms. (d) RMS against charge density ρ of Cu in an FCC lattice. The points are where calculations were carried out and the lines are guides for the eye. The arrow points to the minimum of the RMS and the mesh densities are shown in the legend.

the LDA, we see clear convergence of the surfaces of constant charge density to the I-WP minimal surface.

Aluminum (Al) has the FCC lattice (space group $Fm\bar{3}m$) at standard temperature and pressure. With atomic number 13, aluminum has three valence electrons per atom: $3s^2\,3p$. The lower parabolic-shaped bands lie below the Fermi energy and are, therefore, completely filled and associated mainly with σ bonds formed from two $3s$ electrons with some $3p$ admixture. These lower bands strongly resemble band arising free electrons [47]. The third valence electron occupies the second and third p bands, though with some $3s$ contribution as well. This band has π character along the nearest-neighbor directions.

Figure 6(d) shows the RMS against the charge density for FCC Al as a function of the indicated mesh density. The arrow indicates the minimum value of the RMS. For all FFT meshes, the RMS shows sharp minima in the same region of charge density, with convergence with increasing mesh density and the minimum shifted slightly to lower charge densities, converging to 4.2×10^{-5} Å^{-3}. The converged surface is shown in Fig. 6(a), the F-RD TPMS corresponding to the FCC Al in Fig. 6(b), and the positions of the Al atoms with respect to the TPMS are shown in Fig. 6(c). Thus, for FCC Al with the GGA-PBE XC potential, surfaces of constant charge density converge to the F-RD minimal surface.

Copper (Cu) also has the FCC lattice (space group $Fm\bar{3}m$) at standard temperature and pressure. Copper has atomic number 29 with 11 valence electrons per atom: $3d^{10}\,4s^1$. The $4s$ electrons form wide bands in all high-symmetry directions, but when they cross the $3d$ bands, hybridization splits the s and d bands with the same symmetry near their initial crossing point. The remaining bands are unhybridized and form narrow bands [48] across the Brillouin zone [48].

Figure 7(d) shows the RMS against the charge density for Cu in the FCC lattice as a function of the indicated mesh densities. For all meshes, the RMS shows sharp minima in the same region of constant density, with convergence increasing slightly with the increasing mesh density. The best fit to the F-RD surface, such that the converged minimum appears, is around 6.1×10^{-7}Å^{-3}. The converged surface, the F-RD surface, and the positions of the Cu atoms with respect to the TPMS are shown in Fig. 7(c). Thus, for FCC Cu with the GGA-PBE XC potential, we see convergence of the surfaces of constant charge density to the F-RD minimal surface.

V. SUMMARY

We have shown that for crystalline Na, Al, and Cu, the surfaces of constant ρ converge to the appropriate TPMS as $\rho \to 0$. This is in line with the expectations according to a semiclassical analysis based on the Boltzmann equation. Our theory provides a more versatile calculation of TPMS for crystalline materials than potentials obtained from point charges arranged according to the symmetry of the crystal. Indeed, Mackay [49] has calculated corrections to the leading terms of Schnering and Nesper [26], but these lead to an increase in the RMS when compared to the exact surface [30]. The convergence of the Fourier series representation is discussed in Ref. [50].

DATA AVAILABILITY

The data that support the findings of this article are not publicly available upon publication because it is not technically feasible and/or the cost of preparing, depositing, and hosting the data would be prohibitive within the terms of this research project. The data are available from the authors upon reasonable request.

[1] S. T. Hyde, Z. Blum, T. Landh, S. Lidin, B. W. Ninham, S. Andersson, and K. Larsson, *The Language of Shape: The Role of Curvature in Condensed Matter Physics, Chemistry, and Biology* (Elsevier, Amsterdam, 1997).

[2] A. T. Fomenko and A. A. Tuzhilin, *Elements of the Geometry and Topology of Minimal Surfaces in Three-Dimensional Space* (American, Mathematical Society, Providence, RI, 1991).

[3] M. P. D. Carmo, *Differential Geometry of Curves and Surfaces* (Dover, New York, NY, 2016).

[4] A. H. Schoen, Infinite periodic minimal surfaces without self-intersections, Tech. Rep. TN D-5541 (NASA, Washington, DC, 1970).

[5] H. A. Schwarz, *Gesammelte Mathematische Abhandlungen* (Springer, Berlin, 1890).

[6] S. Torquato and A. Donev, Minimal surfaces and multifunctionality, Proc. R. Soc. London A **460**, 1849 (2004).

[7] O. Al-Ketan and R. K. Al-Rub, Multifunctional mechanical metamaterials based on triply periodic minimal surface lattices, Adv. Eng. Mater. **21**, 1900524 (2019).

[8] J. Feng, J. Fu, X. Yao, and Y. He, Triply periodic minimal surface (TPMS) porous structures: from multi-scale design, precise additive manufacturing to multidisciplinary applications, Int. J. Extrem. Manuf. **4**, 022001 (2022).

[9] S. C. Kapfer, S. T. Hyde, K. Mecke, C. H. Arns, and G. E. Schröder-Turk, Minimal surface scaffold designs for tissue engineering, Biomaterials **32**, 6875 (2011).

[10] R. Pugliese and S. Graziosi, Biomimetic scaffolds using triply periodic minimal surface-based porous structures for biomedical applications, SLAS Technology **28**, 165 (2023).

[11] Y. Huang and L. Zhai, Structural optimization, compressive strength analysis, and application exploration of triply periodic minimal surfaces (TPMS) in interior design Sci. Rep. **15**, 11026 (2025).

[12] S. Cheung, J. Kang, Y. Lin, K. E. Goodson, M. Asheghi, and X. W. Gu, Triply periodic minimal surfaces for thermo-mechanical protection, Sci. Rep. **15**, 1688 (2025).

[13] M. G. Gado, O. Al-Ketan, M. Aziz, R. A. Al-Rub, and S. Ookawara, Triply periodic minimal surface structures: Design, fabrication, 3D printing techniques, state-of-the-art studies, and prospective thermal applications for efficient energy utilization, Energy Technol. **12**, 2301287 (2024).

[14] L. C. Felix, R. Ambekar, R. M. Tromer, C. F. Woellner, V. Rodrigues, P. M. Ajayan, C. S. Tiwary, and D. S. Galvao, Schwarzites and triply periodic minimal surfaces: From pure topology mathematics to macroscale applications, Small 2400351 (2024).

[15] M. Lai, A. Kulak, D. Law, Z. Zhang, F. Meldrum, and D. Riley, Profiting from nature: Macroporous copper with superior mechanical properties, Chem. Commun. **34**, 3547 (2007).

[16] J. W. Galusha, L. R. Richey, J. S. Gardner, J. N. Cha, and M. H. Bartl, Discovery of a diamond-based photonic crystal structure in beetle scales, Phys. Rev. E **77**, 050904(R) (2008).

[17] B. Winter, B. Butz, C. Dieker, G. E. Schröder-Turk, K. Mecke, and E. Spiecker, Coexistence of both gyroid chiralities in individual butterfly wing scales of *Callophrys rubi*, Proc. Natl. Acad. Sci. USA **112**, 12911 (2015).

[18] J. Pérez, A new golden age of minimal surfaces, Notices of the AMS **64**, 347 (2017).

[19] H. Chen and M. Traizet, Stacking disorder in periodic minimal surfaces, SIAM J. Math. Anal. **53**, 855 (2021).

[20] S. Andersson, S. T. Hyde, K. Larsson, and S. Lidin, Minimal surfaces and structures: From inorganic and metal crystals to cell membranes and biopolymers, Chem. Rev. **88**, 221 (1988).

[21] L. Han and S. Che, An overview of materials with triply periodic minimal surfaces and related geometry: From biological structures to self-assembled systems, Adv. Mater. **30**, 1705708 (2018).

[22] S. T. Hyde and S. Andersson, Differential geometry of crystal structure descriptions, relationships and phase transformation, Z. Kristallogr. Cryst. Mater. **170**, 225 (1985).

[23] S. T. Hyde and S. Andersson, The martensite transition and differential geometry, Z. Kristallogr. Cryst. Mater. **174**, 225 (1986).

[24] M. Yin and D. D. Vvedensky, Shape memory effect and the topology of minimal surfaces, Symmetry **16**, 1187 (2024).

[25] H. G. von Schnering and R. Nesper, How nature adapts chemical structures to curved surfaces, Angew. Chem. Int. Ed. Engl. **26**, 1059 (1987).

[26] H. G. von Schnering and R. Nesper, Nodal surfaces of Fourier series: Fundamental invariants of structured matter, Z. Phys. B **83**, 407 (1991).

[27] A. L. Mackay, Crystallographic surfaces, Proc. R. Soc. London A **442**, 47 (1993).

[28] P. J. Gandy, S. Bardhan, A. L. Mackay, and J. Klinowski, Nodal surface approximations to the P, G, D and I-WP triply periodic minimal surfaces, Chem. Phys. Lett. **336**, 187 (2001).

[29] P. J. F. Gandy and J. Klinowski, Geometric quantization of curvature energy in equipotential surfaces of ionic crystals, J. Chem. Phys. **116**, 9431 (2002).

[30] See Supplemental Material at http://link.aps.org/supplemental/10.1103/trld-8v8h for an introduction to minimal surfaces, the data for panels (d) in Figs. 5, 6, 7, and approximations to minimal surfaces obtained from potentials of point charges.

[31] Y. Li and S. Guo, Triply periodic minimal surface using a modified Allen–Cahn equation, Appl. Math. Comput. **295**, 84 (2017).

[32] L. D. Landau and E. M. Lifshitz, *Physical Kinetics*, Vol. 10 of Course of Theoretical Physics (Pergamon, Oxford, 1981).

[33] A. Jüngel, *Transport Equations for Semiconductors*, Lecture Notes in Physics, Vol. 773 (Springer, Berlin, 2009).

[34] F. Reif, *Fundamentals of Statistical and Thermal Physics* (MacGraw-Hill, New York, 1965).

[35] E. Abbena, S. Salamon, and A. Gray, *Modern Differential Geometry of Curves and Surfaces with Mathematica*, 3rd ed. (Chapman and Hall/CRC, Boca Raton, FL, 2006).

[36] G. Kresse and J. Hafner, *Ab initio* molecular dynamics for liquid metals, Phys. Rev. B **47**, 558 (1993).

[37] G. Kresse and J. Furthmüller, Efficient iterative schemes for *ab initio* total-energy calculations using a plane-wave basis set, Phys. Rev. B **54**, 11169 (1996).

[38] G. Kresse and J. Furthmüller, Efficiency of *ab-initio* total energy calculations for metals and semiconductors using a plane-wave basis set, Comput. Mater. Sci. **6**, 15 (1996).

[39] G. Kresse and D. Joubert, From ultrasoft pseudopotentials to the projector augmented-wave method, Phys. Rev. B **59**, 1758 (1999).

[40] H. J. Monkhorst and J. D. Pack, Special points for Brillouin-zone integrations, Phys. Rev. B **13**, 5188 (1976).

[41] J. D. Pack and H. J. Monkhorst, "Special points for Brillouin-zone integrations"–a reply, Phys. Rev. B **16**, 1748 (1977).

[42] W. Kohn and L. J. Sham, Self-consistent equations including exchange and correlation effects, Phys. Rev. **140**, A1133 (1965).

[43] J. P. Perdew, K. Burke, and M. Ernzerhof, Generalized gradient approximation made simple, Phys. Rev. Lett. **77**, 3865 (1996).

[44] A. Jain, S. P. Ong, G. Hautier, W. Chen, W. D. Richards, S. Dacek, S. Cholia, D. Gunter, D. Skinner, G. Ceder, and K. A. Persson, Commentary: The Materials Project: A materials genome approach to accelerating materials innovation, APL Mater. **1**, 011002 (2013).

[45] R. M. Martin, *Electronic Structure: Basic Theory and Practical Methods*, 2nd ed. (Cambridge University Press, Cambridge, 2020).

[46] F. S. Ham, Energy bands of alkali metals. I. Calculated bands, Phys. Rev. **128**, 82 (1962).

[47] B. Segall, Energy bands of aluminum, Phys. Rev. **124**, 1797 (1961).

[48] B. Segall, Fermi surface and energy bands of copper, Phys. Rev. **125**, 109 (1962).

[49] A. L. Mackay, Periodic minimal surfaces from finite element methods, Chem. Phys. Lett. **221**, 317 (1994).

[50] I. Barnes, S. Hyde, and B. Ninham, The caesium chloride zero potential surface is not the schwartz P-surface, J. Phys. Coll. **51**, C7-19 (1990).